

A MICROCLIMATE MODEL FOR NORTHERN APPLICATIONS

by

Glen E. Liston
Universities Space Research Association
Hydrological Sciences Branch, Code 974
NASA/Goddard Space Flight Center
Greenbelt, MD 20771 U.S.A.

Submitted for publication in the preprints volume for the
10th International Northern Research Basins Symposium and Workshop
NORWAY - 1994
Spitsbergen
August 28 to September 3

A MICROCLIMATE MODEL FOR NORTHERN APPLICATIONS

Glen E. Liston
Hydrological Sciences Branch, Code 974
NASA/Goddard Space Flight Center
Greenbelt, Maryland 20771
USA

ABSTRACT

A numerical atmospheric boundary layer model, based on higher-order turbulence closure assumptions, is developed and used to simulate the local advection of momentum, heat, and moisture during the melt of patchy snow covers. The coupled model includes solution of the mass continuity equation, the horizontal and vertical momentum equations, an $E-\epsilon$ turbulence model, an energy equation, and a water vapor conservation equation. Atmospheric buoyancy is accounted for, and a land-surface energy balance model is implemented at the lower boundary.

Model integrations indicate that snow melt processes occurring at micro and local scales produce significant variations in local surface fluxes. Melt energy is found to increase in a largely linear fashion as the fractional snow-covered area decreases. For a given value of fractional snow cover, the available melt energy is nearly invariant with the size of snow patches comprising the snow cover, suggesting that, for the purposes of melt energy computations, the snow patches can be combined into one snow-covered region. In addition, the partitioning of available net solar radiative energy, into upward and downward longwave radiation, and sensible and latent heat fluxes, is found to vary linearly with fractional snow cover.

INTRODUCTION

The interaction between the atmosphere and the surface below has been shown by numerous studies to strongly influence surface hydrologic processes and climate (Charney *et al.* 1977; Shukla and Mintz 1982; Sud *et al.* 1990). Coupled land-atmosphere interaction models commonly assume that the atmospheric surface layer can be treated as horizontally homogeneous over the domain of each model grid cell. In global climate simulations using general circulation models (GCMs), a surface grid cell may typically cover 10^5 km^2 . In a regional atmospheric model, a grid cell typically covers an area of 10 to 100 km^2 . In the natural system, the area covered by these grid elements are clearly inhomogeneous, and these subgrid-scale variations have been shown to significantly influence the surface fluxes of momentum, heat, and moisture (Mahrer and Avissar 1985; Naot and Mahrer 1991; Liston *et al.* 1993).

In light of the importance of subgrid-scale inhomogeneities, attempts have been made to include the affects of spatial variability in land-surface parameterizations used within global and regional climate models. One such approach has been to divide each surface grid cell of the model into homogeneous patches. Under the assumption that the horizontal fluxes between the different patches within the cell are much smaller than the vertical fluxes, patches of the same type are lumped into independent homogeneous elements, creating a grid comprised of a collection of these elements (Avissar and Pielke 1989; Koster and Suarez 1992).

From the perspective of a surface energy balance, one dramatic example of landscape heterogeneity in high latitudes is the patchy configurations of vegetation and snow cover present during the snow melt season. Differences in albedo and roughness length of the two surfaces, in addition to the constraint that the melting snow surface has a temperature of 0°C , contribute to the variations in vertical and horizontal fluxes occurring within the system. Liston (1986) measured the radiative temperatures of snow-free tundra surfaces during snow melt in Arctic Alaska, and found temperatures ranging from 15°C , to as high as 42°C for black lichens, under conditions of clear skies and low wind speeds. The resulting variations in atmospheric temperature and stability over the snow and vegetation surfaces lead to complex air flow patterns and associated momentum, heat, and moisture fluxes. Additional examples of inhomogeneous landscape configurations include transitions from forests to clearings and land to water bodies, and variations in topography.

The horizontal transport of momentum, heat, and moisture, resulting from landscape heterogeneities, is commonly referred to as local advection. When the relatively warm air lying over snow-free ground is advected over a snow-covered

region, an internal boundary layer forms and grows vertically downwind from the leading edge of the snow cover. Further internal boundary layers form and interact as additional vegetation and snow are encountered downwind. As a consequence, large horizontal and vertical gradients develop in the governing atmospheric variables, and lead to variations in the associated fluxes.

In this paper, a model is described and used to study the local advection of momentum, heat, and moisture during the melt of patchy snow covers. In addition, this work is used to assist in developing strategies for including the effects of snow melt-related, subgrid-scale horizontal fluxes in regional and global climate models.

MODEL DESCRIPTION

The following physically-based model has been formulated to describe time-dependent, incompressible, turbulent flows occurring in complex domain configurations. The model is implemented in two-dimensions: horizontal and vertical (flow in the second horizontal dimension is considered homogeneous, and the Coriolis force is assumed negligible). The turbulence closure scheme used in the model has been formulated to include the processes relevant to complex, heterogeneous boundary layer flows containing regions of high shear and variations in stability. Although such simulations are not included in this study, the model is also capable of accounting for complex lower topographic configurations, such as ridges and valleys.

The model is applicable to flow domains ranging from 100 meters to several kilometers in the horizontal, and from 10's of meters to 1 kilometer in the vertical. This domain corresponds to the large microscale and the small mesoscale atmospheric processes as defined by Orlanski (1975). As such, the model simulates fields at the subgrid-scale of regional (mesoscale) atmospheric models, and also serves as a connecting link between point observations and regional model grid values.

General Model Equations

The turbulent flow field is described by the following continuity, and horizontal and vertical momentum equations,

$$\frac{\partial u}{\partial x} + \frac{\partial w}{\partial z} = 0 \quad (1)$$

$$\frac{\partial u}{\partial t} + u \frac{\partial u}{\partial x} + w \frac{\partial u}{\partial z} = -\frac{1}{\rho} \frac{\partial p}{\partial x} + \frac{\partial}{\partial x} \left(v_i \frac{\partial u}{\partial x} \right) + \frac{\partial}{\partial z} \left(v_i \frac{\partial u}{\partial z} \right) \quad (2)$$

$$\frac{\partial w}{\partial t} + u \frac{\partial w}{\partial x} + w \frac{\partial w}{\partial z} = -\frac{1}{\rho} \frac{\partial p}{\partial z} + \frac{\partial}{\partial x} \left(v_t \frac{\partial w}{\partial x} \right) + \frac{\partial}{\partial z} \left(v_t \frac{\partial w}{\partial z} \right) \quad (3)$$

where u and w are the velocity components in the x (horizontal) and z (vertical) directions, respectively; p is pressure; t is time; and ρ is the air density. The turbulent viscosity, v_t , is

$$v_t = c_\mu \frac{E^2}{\varepsilon} \quad (4)$$

where c_μ is an empirical constant (Jones and Launder 1972).

The turbulent kinetic energy, E , and the rate of dissipation of turbulent kinetic energy, ε , are given by

$$\frac{\partial E}{\partial t} + u \frac{\partial E}{\partial x} + w \frac{\partial E}{\partial z} = \frac{\partial}{\partial x} \left(\frac{v_t}{\sigma_E} \frac{\partial E}{\partial x} \right) + \frac{\partial}{\partial z} \left(\frac{v_t}{\sigma_E} \frac{\partial E}{\partial z} \right) + S_S + S_B - \varepsilon \quad (5)$$

$$\begin{aligned} \frac{\partial \varepsilon}{\partial t} + u \frac{\partial \varepsilon}{\partial x} + w \frac{\partial \varepsilon}{\partial z} = & \frac{\partial}{\partial x} \left(\frac{v_t}{\sigma_\varepsilon} \frac{\partial \varepsilon}{\partial x} \right) + \frac{\partial}{\partial z} \left(\frac{v_t}{\sigma_\varepsilon} \frac{\partial \varepsilon}{\partial z} \right) \\ & + c_{1\varepsilon} \frac{\varepsilon}{E} (S_S + c_{3\varepsilon} S_B) - c_{2\varepsilon} \frac{\varepsilon^2}{E} \end{aligned} \quad (6)$$

where $c_{1\varepsilon}$, $c_{2\varepsilon}$, $c_{3\varepsilon}$, σ_E , and σ_ε are empirical constants (Launder and Spalding 1974; Rodi 1984). S_S is a source term resulting from shear,

$$S_S = v_t \left(\frac{\partial u}{\partial z} - \frac{\partial w}{\partial x} \right)^2 \quad (7)$$

and S_B is a buoyancy source term described by

$$S_B = g_z \frac{v_t}{\sigma_t} \frac{1}{\theta} \frac{\partial \theta}{\partial z} \quad (8)$$

where g_z is the gravitational acceleration, σ_t is the turbulent Prandtl number, and θ is the potential temperature.

The energy conservation equation that describes the evolution of potential temperature, θ , is

$$\frac{\partial \theta}{\partial t} + u \frac{\partial \theta}{\partial x} + w \frac{\partial \theta}{\partial z} = \frac{\partial}{\partial x} \left(\Gamma_t \frac{\partial \theta}{\partial x} \right) + \frac{\partial}{\partial z} \left(\Gamma_t \frac{\partial \theta}{\partial z} \right) \quad (9)$$

where Γ_t is the turbulent diffusivity for heat. The conservation equation for the vapor

phase specific humidity, or mass of water vapor per unit mass of air, q_v , is

$$\frac{\partial q_v}{\partial t} + u \frac{\partial q_v}{\partial x} + w \frac{\partial q_v}{\partial z} = \frac{\partial}{\partial x} \left(\Gamma_t \frac{\partial q_v}{\partial x} \right) + \frac{\partial}{\partial z} \left(\Gamma_t \frac{\partial q_v}{\partial z} \right) \quad (10)$$

where the turbulent diffusivity for mass and heat have been assumed equal.

The turbulent Prandtl number is given by the ratio of the turbulent viscosity, ν_t , to the turbulent diffusivity, Γ_t ,

$$\sigma_t = \frac{\nu_t}{\Gamma_t} \quad (11)$$

and is assumed to take the form adopted by Bartzis *et al.* (1991),

$$\sigma_t = \begin{cases} \text{Pr} \frac{(1 - 9 \text{ Ri})^{-1/2}}{(1 - 15 \text{ Ri})^{-1/4}} & \text{Ri} < 0 \\ \text{Pr} & \text{Ri} \geq 0 \end{cases} \quad (12)$$

where the molecular Prandtl number, $\text{Pr} = \mu c_p / \lambda$; μ is the molecular viscosity, c_p is the specific heat of air at constant pressure, and λ is the thermal conductivity. The Richardson number, Ri , is given by

$$\text{Ri} = - \frac{g_z}{\theta} \frac{\partial \theta / \partial z}{(\partial u / \partial z)^2} \quad (13)$$

The potential temperature is related to the actual temperature, T , through the virtual temperature. In this study the difference between the potential and actual temperature has been assumed negligible.

The empirical constants used in the model are considered generally universal, and are assumed to be (ASCE 1988; Liston *et al.* 1993): $c_\mu = 0.03$, $c_{1\varepsilon} = 1.16$, $c_{2\varepsilon} = 1.92$, $\sigma_E = 1.0$, $\sigma_\varepsilon = 1.3$, and

$$c_{3\varepsilon} = \begin{cases} 1 & (S_B > 0) \\ 0 & (S_B \leq 0) \end{cases} \quad (14)$$

For the case of neutrally buoyant conditions, the above model has been found to successfully simulate separated atmospheric surface-layer flows (Liston *et al.* 1993).

Boundary Conditions

The incoming velocity profile is assumed to be

$$u = u_* / \kappa \ln (z/z_0) \quad (15)$$

where u_* is the shear velocity, κ is von Karman's constant, and z_0 is the roughness height. This logarithmic profile is also used as a lower boundary condition for the horizontal velocity. The incoming and lower surface vertical velocities are set to zero. Incoming profiles of E and ϵ are given by

$$E = \frac{u_*^2}{\sqrt{C_u}} \quad (16)$$

(Frost *et al.* 1975) and

$$\epsilon = \frac{u_*^3}{\kappa z} \quad (17)$$

(Panofsky and Dutton 1984) respectively, and are also used as lower boundary conditions for these variables.

The inflow boundary conditions for potential temperature and specific humidity are obtained from meteorological station observations of air temperature and relative humidity or vapor pressure. Confining the region of the inflow boundary to adiabatic transformations leads to a potential temperature which is constant with height and, in this study, is assumed to be equal to the observed air temperature, T_r , at reference height, z_r . The specific humidity, q_{vr} , at the reference height, is given by computing the vapor pressure, e_r , according to

$$e_r = RH * 10^{\left(11.40 - \frac{2353}{T_r}\right)} \quad (18)$$

where RH is the observed relative humidity (expressed as a fraction), and

$$q_{vr} = 0.622 \frac{e_r}{p_r} \quad (19)$$

where a representative atmospheric pressure, p_r , for the location of interest is given by

$$p_r = p_0 \exp\left(-\frac{Z_g}{H}\right) \quad (20)$$

where p_0 is a reference sea level pressure (101,300 Pa), H is the scale height of the atmosphere (≈ 8000 m), and Z_g is the elevation of the study site (Wallace and Hobbs 1977).

The inflow specific humidity profile is obtained from

$$q_v = q_{vr} - \frac{E_v}{\kappa u_* \rho} \ln \left(\frac{z}{z_r} \right) \quad (21)$$

where E_v is the evaporation rate (Brutsaert and Kustas 1985), determined from the surface latent heat flux, Q_e , according to

$$E_v = - \frac{Q_e}{L_v} \quad (22)$$

where L_v is the latent heat of vaporization.

At the lower boundary, the surface temperature boundary condition is computed by implementing a complete surface energy balance, as described in the next section. The vapor pressure at the lower boundary is

$$e_0 = \beta * 10^{\left(11.40 - \frac{2353}{T_0}\right)} \quad (23)$$

where T_0 is the surface temperature, and β is the soil moisture fraction (0 - 1) obtained from a soil hydrology model; in this study β is set equal to one. Thus, the specific humidity at the surface can be obtained by substituting e_0 into Equation (19).

The upper and outflow boundary conditions for u , w , E , ε , θ , and q_v , and the conditions at all boundaries for p , are defined to be

$$\frac{\partial \Omega}{\partial n} = 0 \quad (24)$$

where Ω is the dependent variable of interest, and n is oriented normal to the boundary.

Initial conditions for model integrations are obtained by distributing the inflow boundary conditions throughout the flow domain. The integrations then proceed until an equilibrium state is obtained during the period of interest.

Surface Energy Balance

To determine the surface temperature boundary condition, a complete energy balance is computed at the surface. The surface energy balance equation is

$$(1 - \alpha_s) Q_{si} + Q_{li} + Q_{le} + Q_h + Q_e + Q_c = Q_m \quad (25)$$

where Q_{si} is the solar radiation reaching the surface of the earth, Q_{li} is the incoming longwave radiation, Q_{le} is the emitted longwave radiation, Q_h is the turbulent exchange of sensible heat, Q_e is the turbulent exchange of latent heat, Q_c is the energy transport due to conduction, Q_m is the energy flux available for melt, and α_s is the albedo of the

surface. Energy transports towards the surface are defined to be positive.

The solar radiation striking a horizontal surface, Q_{si} , is given by

$$Q_{si} = S^* \Psi \sin \omega \quad (26)$$

where S^* is the solar irradiance at the top of the atmosphere striking a surface normal to the solar beam (1370 W m^{-2}) (Kyle *et al.* 1985), and Ψ is the net sky transmissivity, or the fraction of solar radiation that makes it to the surface. The solar elevation angle, ω , is defined to be

$$\sin \omega = \sin \delta \sin \phi + \cos \delta \cos \phi \cos \tau \quad (27)$$

where ϕ is latitude, τ is the hour angle measured from local solar noon, and δ is the solar declination angle approximated by

$$\delta = \phi_T \cos \left(2\pi \left(\frac{d - d_r}{d_y} \right) \right) \quad (28)$$

where ϕ_T is the latitude of the Tropic of Cancer (23.45° N), d is the Gregorian Day, d_r is the day of the summer solstice (173), and d_y is the average number of days in a year (365.25).

To account for the scattering, absorption, and reflection of short-wave radiation by clouds, the solar radiation is scaled according to

$$\Psi = (0.6 - 0.2 \sin \omega) (1.0 - 0.5 \sigma_c) \quad (29)$$

where σ_c represents the fraction of cloud cover (Burridge and Gadd 1974).

An analytical downward longwave radiation equation which considers clear skies and standard atmospheric conditions has been developed by Brutsaert (1975). To correct apparent deficiencies in this formulation at air temperatures below 0° C (Aase and Idso 1978), Satterlund (1979) suggested the empirical description

$$Q_{li} = 1.08 \left(1 - \exp \left(- (0.01 e_r)^{T_r/2016} \right) \right) \sigma T_r^4 \quad (30)$$

where the atmospheric vapor pressure, e_r (Pa), is given by Equation (18). In the current study no attempt has been made to modify this formulation for Q_{li} to account for the presence of clouds.

The longwave radiation emitted by the snow surface is computed under the assumption that snow emits as a grey body,

$$Q_{le} = -\epsilon_s \sigma T_0^4 \quad (31)$$

where T_0 is the snow surface temperature, σ is the Stefan-Boltzmann constant, and ϵ_s is the surface emissivity, assumed to be 0.98.

The turbulent exchange of sensible and latent heat, Q_h and Q_e , respectively, are given by (Price and Dunne 1976)

$$Q_h = \rho c_p D_h \zeta (T_r - T_0) \quad (32)$$

$$Q_e = \rho L_v D_e \zeta \left(0.622 \frac{e_r - e_0}{p_r} \right) \quad (33)$$

where ζ is a non-dimensional stability function. D_h and D_e are exchange coefficients for sensible and latent heat, respectively,

$$D_h = D_e = \frac{\kappa^2 u_r}{(\ln(z_r / z_0))^2} \quad (34)$$

where u_r is the wind speed at reference height z_r . Under stable atmospheric conditions the stability function, ζ , modifies the turbulent fluxes through the formula

$$\zeta = 1 / (1 + 10\text{Ri}) \quad (35)$$

where the Richardson number, Ri , is given by Equation (13).

Heat conduction flux at the surface is

$$Q_c = -k_g \left. \frac{dT_g}{dz} \right|_0 \quad (36)$$

where T_g is the ground temperature and k_g is the effective thermal conductivity of the vegetation/soil matrix. In this study the conductive flux is assumed negligible.

To solve the system of equations for the surface temperature, the equations are cast in the form: $f(T_0) = 0$, and solved iteratively for T_0 using the Newton-Raphson method. In the presence of snow, surface temperatures $T_0 > 0$ °C, resulting from the surface energy balance, indicates that energy is available for melting, Q_m . The amount available is then computed by setting the surface temperature to 0 °C and recomputing the surface energy balance. A similar procedure is adopted to compute the energy available to freeze, Q_f , liquid water present.

Numerical Solution Procedure

Equations (1-14), in conjunction with the boundary conditions found in Equations (15-36), comprise the coupled, nonlinear system of equations which models the unsteady,

two-dimensional turbulent velocity, temperature, and specific humidity fields. The SIMPLER (Semi-Implicit Method for Pressure-Linked Equations, Revised) finite control volume algorithm described by Patankar (1980) is used to solve the system of partial differential transport equations.

COMPUTATIONAL RESULTS

In what follows the above planetary boundary layer model is used to describe land-atmosphere interactions during the melt of patchy snow covers. The domain of interest covers a horizontal distance of 10 km, and a vertical height of 1 km. There are 200 horizontal grid cells with a spacing of 50 m, and 40 vertical levels with a spacing of 0.05 m at the ground, and stretched by a factor of 1.23 to reach 160 m at the top of the domain.

The results of nine simulations of various snow-vegetation patterns over the domain will be presented (Figure 1). Cases A, B, C, and D represent the condition of 50% snow cover, where the size of the snow patches making up the snow cover varies from 0.5 to 4 km. All of the snow-vegetation patterns used in this study include a 1 km snow coverage at the inflow boundary (left-hand-side of the figure), and a 1 km segment of exposed vegetation at the outflow boundary (not shown in Figure 1). Cases 1 through 6 represent a gradual increase in the size of the vegetation cover upwind of the snow patch of interest. As such, these cases correspond to a decrease in snow covered area within the domain, with snow cover ranging from 88 to 6%. Cases A and 3 are identical.

In the simulations, the difference between snow and vegetation is defined through the roughness length and the albedo. The roughness length of snow is assumed to equal 0.001 m, and that of the vegetation (tundra) is 0.035 m. The temperature of the melting snow surface is 0 °C, with an albedo of 0.5. The albedo of the vegetation is defined to be 0.15. The energy balance computations are performed for the following case: the latitude is 68 degrees North, during solar noon, on May 15, and under a cloud free sky. The upwind boundary reference temperature, relative humidity, and wind velocity, at 2 m height, are defined to be 0 °C, 50%, and 2 m s⁻¹, respectively. These conditions represent an extreme case from the perspective of snow melt; on May 15 the solar radiation is near its peak, and incoming solar radiation is reduced during other times of the day and under other cloud scenarios.

Figure 2 displays the air temperature field (°C) for Case B. Wind flow is from left to right. The heat islands produced by the exposed vegetation are evident, as are the merging temperature contours downwind of the vegetation. These heat plumes are

Figure 1: Snow-vegetation patterns used in model integrations.

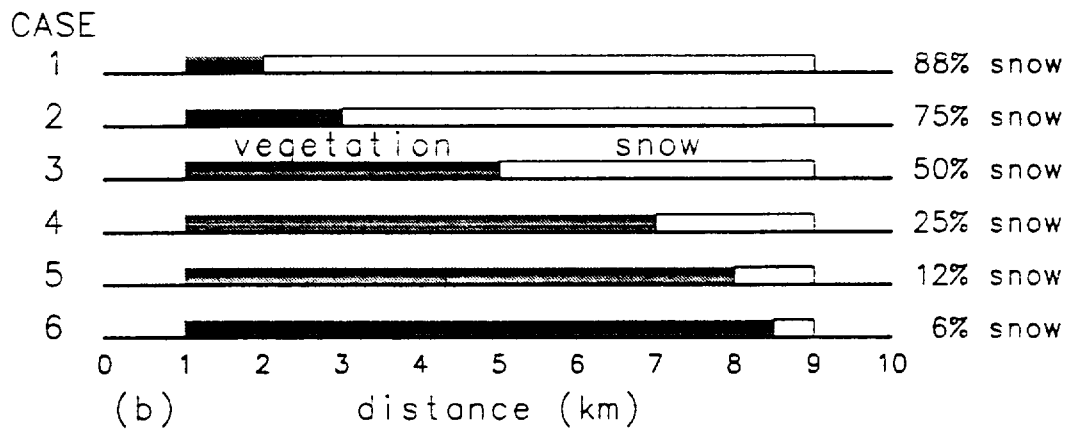
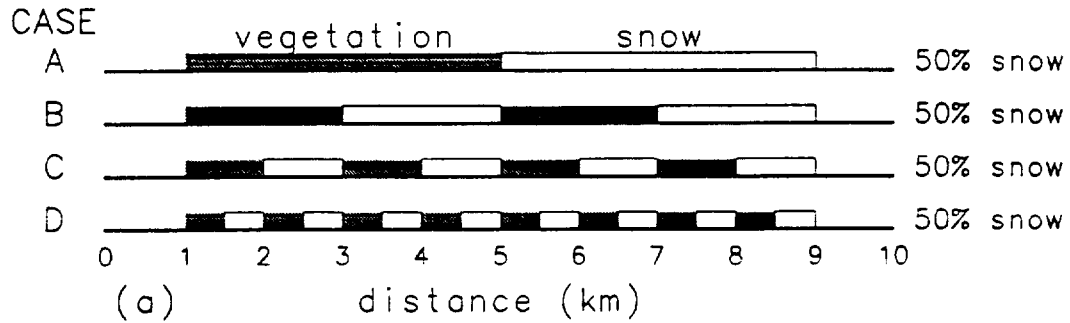
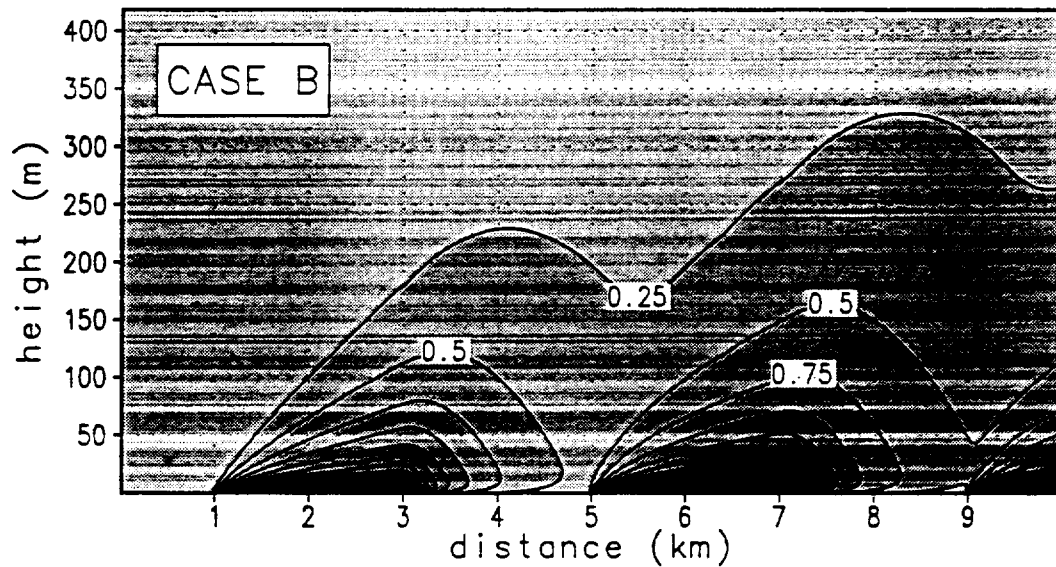


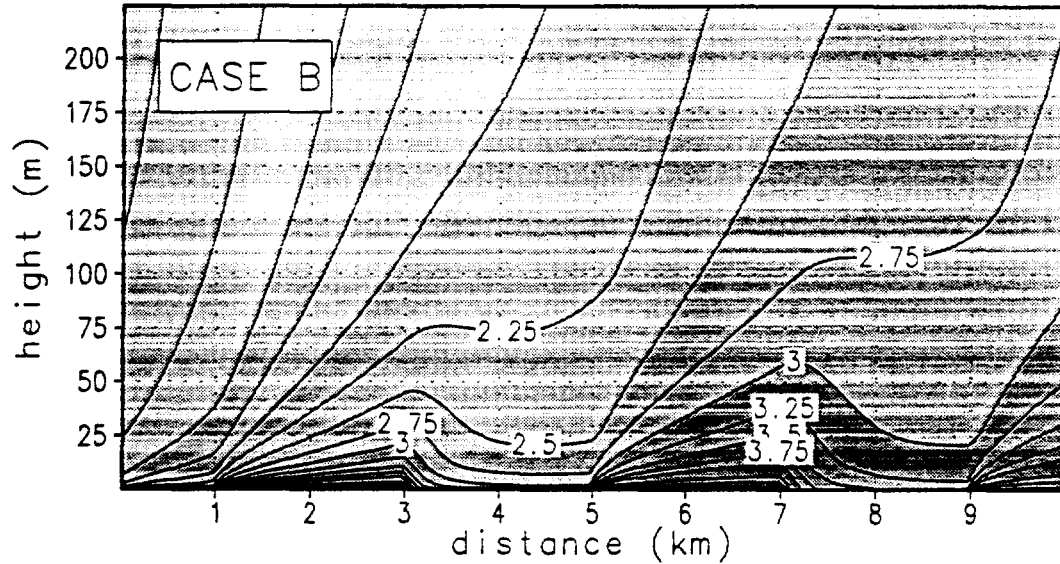
Figure 2: Model simulated air temperature ($^{\circ}\text{C}$) field for Case B.



transported downwind and produce higher air temperatures over the snow-covered areas. These temperatures decrease with downwind distance from the leading edge of each snow patch, and they increase with the number of upwind vegetation elements.

Figure 3 shows the computed specific humidity field (g kg^{-1}) for Case B. The presence of the vegetation-snow patterns strongly influence the local atmospheric water vapor distribution. Simulations of the other vegetation-snow patterns (Figure 1) produce similar qualitative results for both temperature and specific humidity.

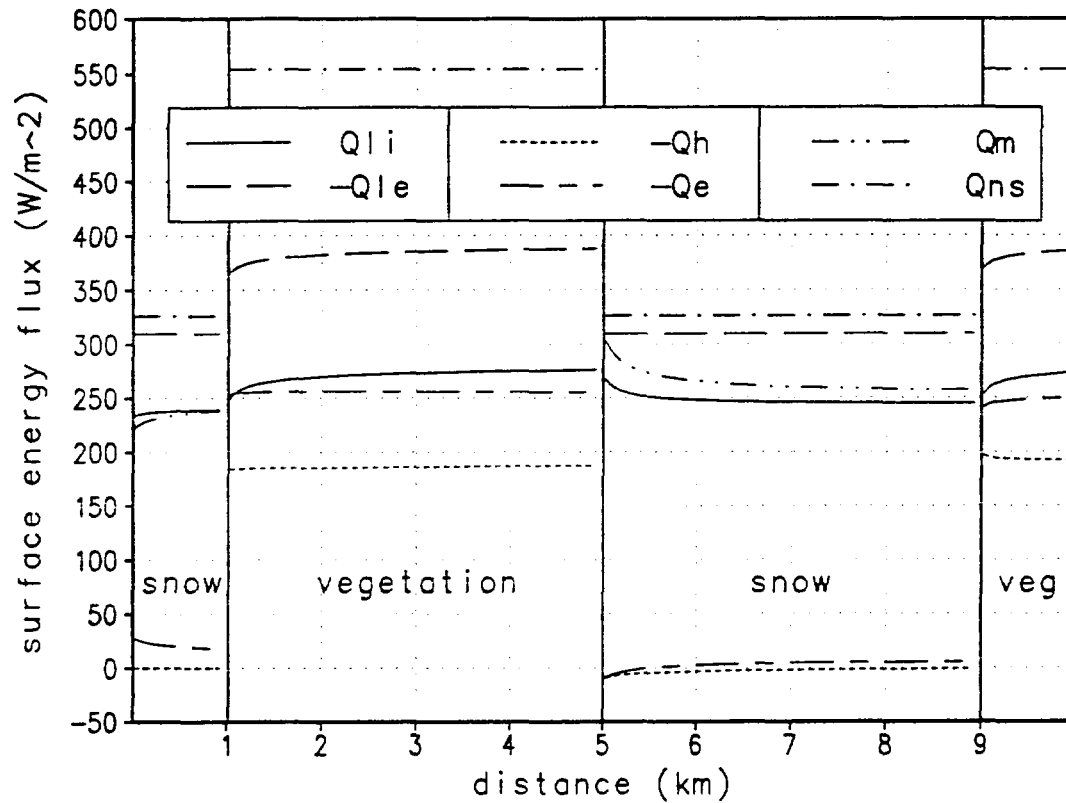
Figure 3: Model simulated specific humidity (g kg^{-1}) field for Case B.



The surface energy balance differs widely for the vegetation and snow-covered areas. Results of the energy balance computations for Case A (Case 3) are found in Figure 4. The net solar radiative flux at the surface, Q_{ns} , differs between the vegetation and snow due to their differences in albedo. Incoming longwave radiation, Q_{li} , follows the air temperature, and is continuous over the vegetation-snow boundaries. The negative of the emitted longwave radiation, $-Q_{le}$, follows the surface temperature. It is constant over the melting snow, and discontinuous at the vegetation-snow boundaries. These radiative energy fluxes are similar to those measured by Hinzman (1990) during snow melt in Arctic Alaska.

Under the conditions of this simulation, the negative of the sensible heat flux, $-Q_h$, and latent heat flux, $-Q_e$, are minimal over snow (Figure 4). These terms are positive, much larger and roughly constant, approximately 180 W m^{-2} for $-Q_h$ and 250 W m^{-2} for $-Q_e$, over the vegetation portion of the domain. Additional model integrations show that the inflow relative humidity plays a key role in governing these values of sensible and latent heat. The energy available to melt snow, Q_m , is only computed over the snow-covered regions, and it decreases with distance from the leading edge of the snow patch.

Figure 4: Model simulated surface energy balance components for Case A (Case 3).

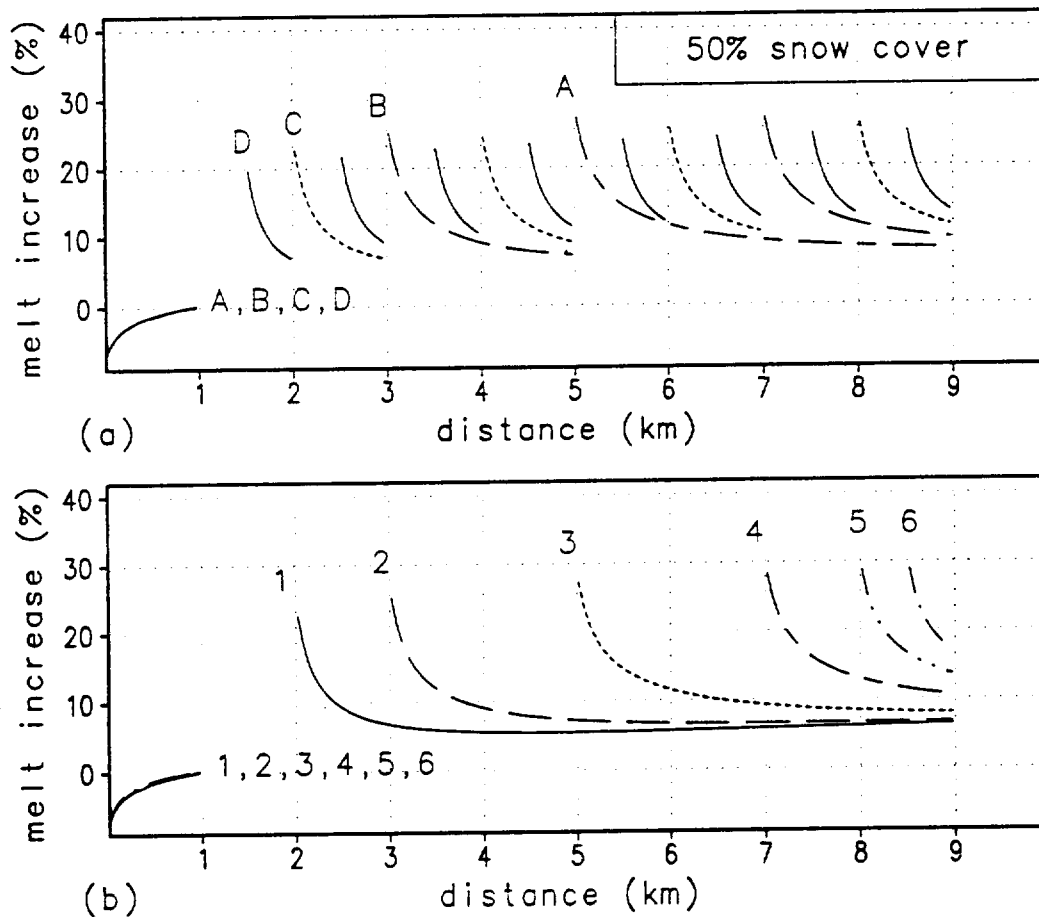


The melting energy for each of the Cases A – D, and 1 – 6, are plotted in Figures 5a, and 5b, respectively. The length and locations of these curves correspond to the snow-covered area for each case. The melting energy over each snow patch was nondimensionalized by subtracting the melt energy at the trailing edge of the inflow snow patch, dividing the result by the same inflow melt energy, and expressing the final value as a percent. These figures show the enhanced melt energy resulting from the local advection of momentum, heat, and moisture. Consider, for example, Case A (Case 3). At the leading edge of the snow patch, the melting energy is 28% higher than that present at the inflow snow patch. This increase in energy decreases to 8% at the trailing edge of the snow cover, in response to the presence of the lower-temperature snow surface. The other cases are qualitatively similar.

Integration of the curves in Figure 5, to obtain averages over the flow domain, allows a quantitative analysis of the effect that snow patch size and fractional snow-covered area has on snow melt. Figure 6a describes the increase in melt energy as the ratio of snow patch size to total area decreases, for the case of 50% snow cover (Cases A – D). As the snow patch size decreases from 4 to 0.5 km (or the ratio of snow patch size to total area goes from 50 to 6%), the melt energy increases by 4%. Figure 6b

illustrates the increase in melt energy, from 7 to 21%, as the snow-covered area reduces from 88 to 6% (Cases 1 – 6). The simulations show these snow cover and snow melt relationships to be largely linear over the range of cases studied. Figure 6 suggests that as the ratio of patch size to total area (Figure 6a), and the snow covered area (Figure 6a), falls below 10%, this linearity begins to break down. In addition, this figure indicates that in the computation of the energy available to melt the snow, the total fractional snow cover is of primary importance, and that the distribution of the snow cover across the domain, or the patchiness, is secondary.

Figure 5: Increase in snow melt energy, nondimensionalized by the melt energy at the trailing edge of the inflow snow patch for (a) Cases A – D, and (b) Cases 1 – 6.



Model simulations for snow-vegetation patterns similar to those shown in Figure 1, but for a 1 km horizontal domain with patches ranging from 50 to 400 m, show comparable results to those found in Figure 6. In this case, the melt energy increased by 3% as the snow patch size decreased from 400 to 50 m, and the melt increased from 4 to 20% as the snow-covered area decreased from 88 to 6%. The linearity of the snow

cover and snow melt relationships in these simulations closely parallel those for the larger domain computations.

Figure 6: Average melt energy computed from profiles in Figure 5: (a) the effect of snow patch size on melt energy for the condition of 50% snow cover (Cases A – D), and (b) the effect of fractional snow covered area on melt energy (Cases 1 – 6).

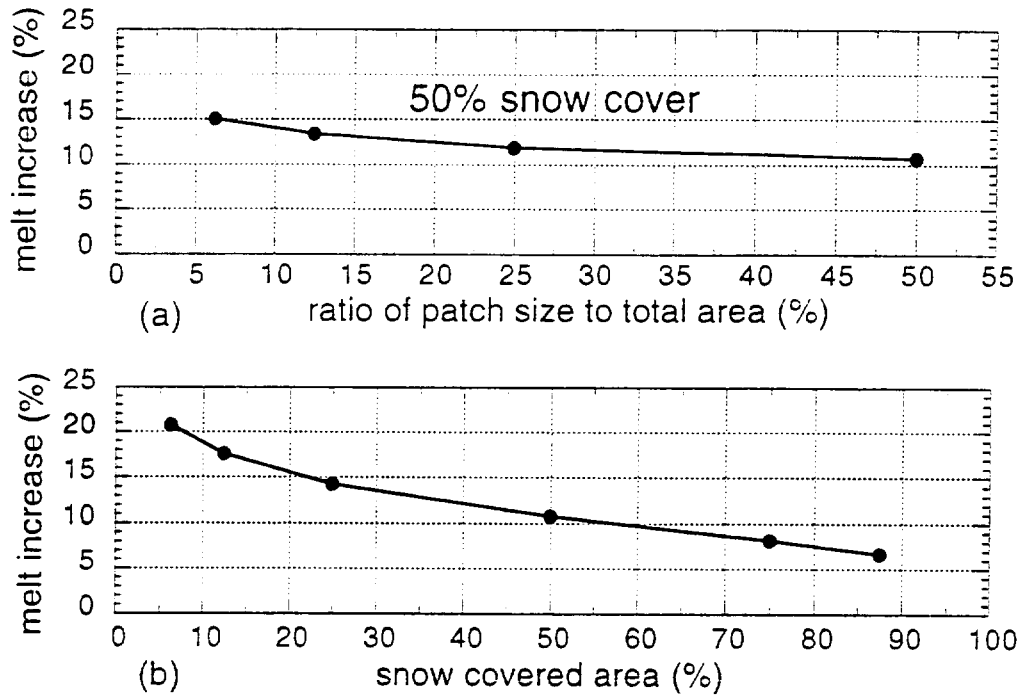
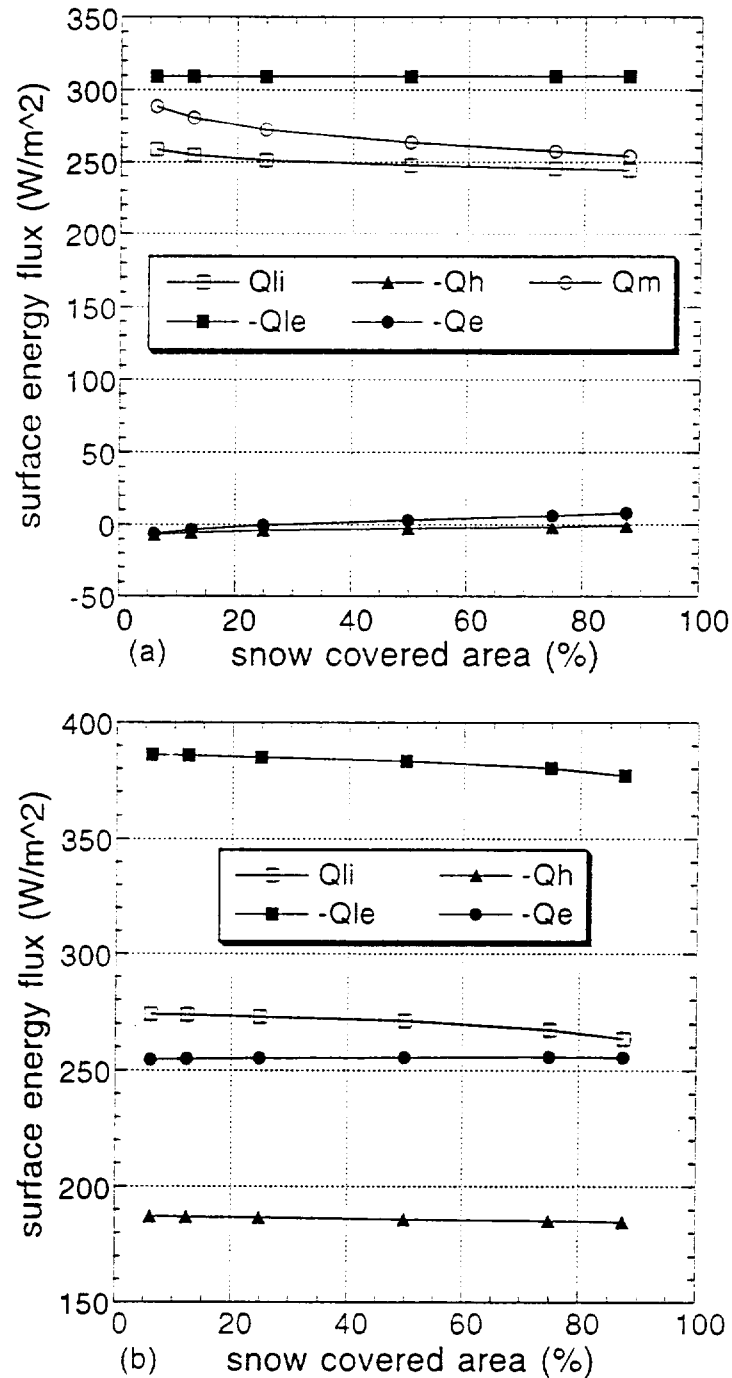


Figure 7 displays the results of integrating the surface fluxes (see Figure 4) over the snow-covered (Figure 7a) and the vegetation-covered (Figure 7b) regions of the domain, for Cases 1 – 6. Over the snow-covered areas the incoming longwave radiation, melt energy, and sensible and latent heat are nonconstant and slightly nonlinear as the fractional snow cover varies. The net solar radiation is constant and equal to 326 W m^{-2} over the snow (not shown in Figure 7a). In these simulations, the increase in melt energy closely parallels, and is largely the consequence of, increased incoming longwave radiation resulting from the advection of heat from the upwind vegetation patches (see Figure 2). Over the vegetation-covered regions the incoming and emitted longwave radiation are nonconstant and slightly nonlinear, while the sensible and latent heat are invariant with snow-covered area. The net solar radiation over the vegetation is constant and equal to 554 W m^{-2} (not shown in Figure 7b).

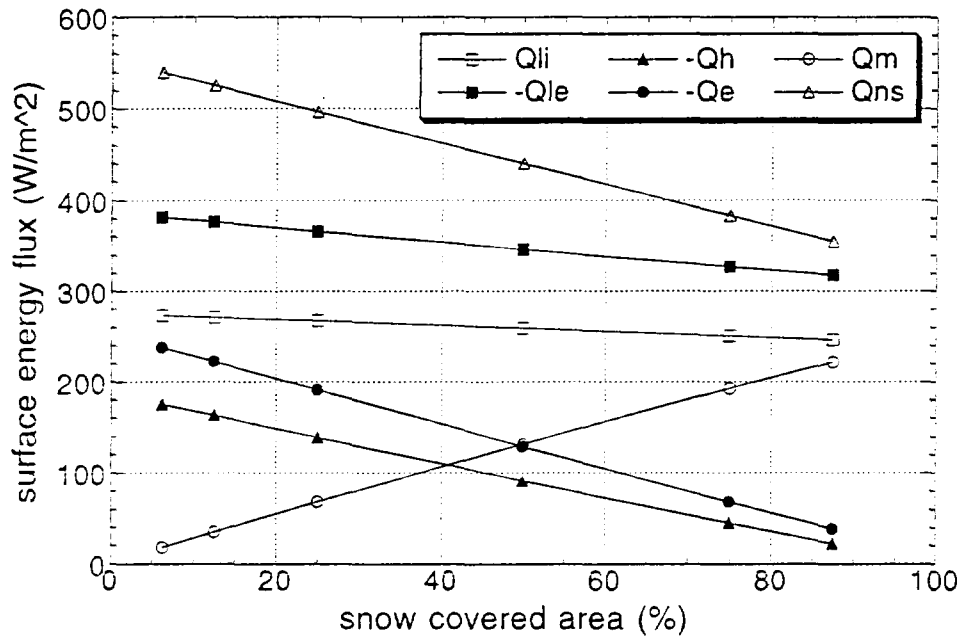
The results of integrating the surface fluxes over the entire domain (combining both snow and vegetated regions), for Cases 1 – 6, are given in Figure 8. In addition to the expected linear increase in net solar radiation as snow-covered area decreases, the other

Figure 7: Average surface energy flux dependence on snow-covered area for Cases 1 – 6: (a) over snow, and (b) over vegetation.



energy balance components display strong linear relationships to fractional snow cover. This implies that the partitioning of the available solar radiative energy varies linearly with snow-covered area, and that the effects of local advection, during the melt of patchy snow cover, can be accounted for through knowledge of the fractional snow and

Figure 8: Average surface energy fluxes over the entire domain (combining both snow and vegetated regions), for Cases 1 – 6.



vegetation cover. While the fractional snow cover is expected to play a key role in the partitioning of available energy into upward and downward longwave radiation, and sensible and latent heat fluxes, other meteorological factors, such as wind speed, are expected to be important.

DISCUSSION AND CONCLUSIONS

Regional and global atmospheric models generally resolve grid-average surface fields of wind speed, air temperature, vapor pressure, and surface fluxes; the details of any subgrid-scale flow features are unaccounted for. This leads to the question of the role that local advection plays in modifying the surface fluxes at subgrid-scales. An atmospheric boundary layer model has been developed and used to study the local advection of momentum, heat, and moisture during snow melt. The degree to which local advection influences snow melt will be a function of several factors, including wind speed, surface roughness and albedo, cloud cover, and vapor pressure. The influence of local advection on modifying the surface energy balance during midday melting is seen in the variations of energy fluxes over the snow-covered areas and the vegetation-covered areas of Figure 4. The variations are most significant at the leading edges of the vegetation and snow cover patches, and are much less dramatic than the differences between the average fluxes computed over the individual covers of snow

and vegetation. Numerous investigators have noted this dramatic increase of net radiation, when the snow surface is replaced by tundra, during snow melt in the arctic (e.g., Weller and Holmgren 1974; Hinzman 1990).

For the purposes of computing grid-average surface fluxes during snow melt in regional atmospheric models, the results of this study indicate that each regional model surface grid cell can be divided into homogeneous subdomains of snow and vegetation. In addition, since the influence of patch size (or patchiness) has been found to be much less significant than that of total snow covered area, all of the subdomains of the same type can be combined into homogeneous surface elements. For this case of snow and vegetative surfaces, all of the snow patches within each regional model grid cell can be lumped together to form one large snow-covered region, leading to a measure of the areal fraction of snow and vegetation within each grid cell. Energy balance computations can be performed over each of the surface types, and the resulting fluxes can be areally weighted and combined, with an additional local advection-related weighting proportional to the fractional snow cover, to allocate the total energy flux partitioning within each surface grid cell. The linear relationship between snow melt energy and fractional snow cover has been found to break down as the snow-covered area drops below 10%.

Such linear relationships between snow-vegetation-atmosphere interactions has significant implications for the development of land surface parameterizations for use in regional and global atmospheric models. In addition, these findings lend support to the approaches of Avissar and Pielke (1989) in their regional modeling, and Koster and Suarez (1992) in their general circulation modeling; they divide each model grid into subgrid areas composed of several separate vegetation types, permanent ice cover, and open water. The findings of the current study suggest that a similar accounting for the fractional snow-covered area will assist in providing a realistic simulation of surface fluxes under conditions of patchy snow covers.

The suggested importance of accounting for local advection when computing regional model grid-averaged surface fluxes during the melt of patchy snow covers has been based on the limited simulations presented in this study. The inclusion of a full diurnal cycle in the integrations is expected to reduce the effects illustrated here for the case of snow melt during solar noon. Further simulations are also necessary to establish the influences of other landscape heterogeneities such as transitions from forests to clearings, and topographic variations.

Beyond indicating the appropriateness of linearly aggregating regional atmospheric model subgrid-scale surface fluxes during snow melt, this study has highlighted the

need to quantify the fractional snow-covered area during the evolution of seasonal snow covers. Such a description of snow areal extent is expected to result primarily from data collected by airborne and satellite sensors, but would also benefit from the combined input of meteorological data, ground-based snow observations, digital elevation data, and forest canopy data sets. Realistically incorporating snow cover in regional atmospheric models and GCMs is expected to improve the subsequent analysis and simulation of land-atmosphere interactions, weather, and climate.

ACKNOWLEDGEMENTS

The author wishes to thank Drs. Max Suarez, Dorothy Hall, and Al Chang of NASA/Goddard Space Flight Center for their comments and support during this modeling effort.

REFERENCES

- ASCE (1988) Turbulence modeling of surface water flow and transport: Part IV. *J. Hyd. Engr.* 114, pp. 1034-1051.
- Aase, J.K., and Idso, S.B. (1978) A comparison of two formula types for calculating long-wave radiation from the atmosphere. *Water Resour. Res.* 14, pp. 623-625.
- Avissar, R., and Pielke, R.A. (1989) A parameterization of heterogeneous land surfaces for atmospheric numerical models and its impact on regional meteorology. *Mon. Weather Rev.* 117, pp. 2113-2136.
- Bartzis, J.G., Venetsanos, A.G., Varvayanni, M., Catsaros, N., and Megaritou, A. (1991) ADREA-I: a three-dimensional transient transport code for complex terrain and other applications. *Nuclear Tech.* 94, pp. 135-148.
- Brutsaert, W. (1975) On a derivable formula for long-wave radiation from clear skies. *Water Resour. Res.* 11, pp. 742-744.
- Brutsaert, W., and Kustas, W.P. (1985) Evaporation and humidity for neutral conditions over rugged hilly terrain. *J. Climate and Appl. Met.* 24, pp. 915-923.
- Burridge, D.M., and Gadd, A.J. (1974) The Meteorological Office operational 10 level numerical weather prediction model (December 1974). British Met. Office Tech. Notes Nos. 12 and 48. London Rd., Bracknell, Berkshire, RG12 2SZ, England, 57 pp.
- Charney, J.G., Quirk, W.J., Chow, S.H., and Kornfield, J. (1977) A comparative study of the effects of albedo change on drought in semi-arid regions. *J. Atmos. Sci.* 34, pp. 1366-1385.
- Frost, W., Harper, W.L., and Fichtl, G.H. (1975) Analysis of atmospheric flow over a surface protrusion using the turbulence kinetic energy equation. *Boundary-Layer Meteorol.* 8, pp. 401-417.
- Hinzman, D.L. (1990) The interdependence of the thermal and hydrological processes of an arctic watershed and their response to climatic change. Doctoral Dissertation, University of Alaska, Fairbanks.
- Jones, W.P., and Launder, B.E. (1972) The prediction of laminarization with a two-equation model of turbulence. *Int. J. Heat Mass Transfer* 15, pp. 301-314.
- Koster, R.D., and Suarez, M.J. (1992) Modeling the land surface boundary in climate models as a composite of independent vegetation stands. *J. Geophys. Res.* 97 (D3), pp. 2697-2715.

- Kyle, H.L., Ardanuy, P.E., and Hurley, E.J. (1985) The status of the Nimbus-7 earth-radiation-budget data set. *Bull. Am. Meteor. Soc.* 66, pp. 1378-1388.
- Launder, B.E., and Spalding, D.B. (1974) The numerical computation of turbulent flow. *Comp. Meth. in Appl. Mech. and Eng.* 3, pp. 269-289.
- Liston, G.E. (1986) Seasonal snowcover of the foothills region of Alaska's arctic slope: a survey of properties and processes. M.S. Thesis, University of Alaska, Fairbanks.
- Liston, G.E., Brown, R.L., and Dent, J. (1993) Application of the E- ϵ turbulence closure model to separated atmospheric surface-layer flows. *Boundary-Layer Meteorol.* 66, pp. 281-301.
- Mahrer, Y., and Avissar, R. (1985) A numerical study of the effects of soil surface shape upon the soil temperature and moisture regimes. *Soil Science* 139, pp. 483-490.
- Naot, O., and Mahrer, Y. (1991) Two-dimensional microclimate distribution within and above a crop canopy in an arid environment: modeling and observational studies. *Boundary-Layer Meteorol.* 56, pp. 223-244.
- Orlanski, I. (1975) A rational subdivision of scales for atmospheric processes. *Bull. Am. Met. Soc.* 56, pp. 527-530.
- Panofsky, H.A., and Dutton, J.A. (1984) *Atmospheric Turbulence*, John Wiley and Sons, New York.
- Patankar, S.V. (1980) *Numerical Heat Transfer and Fluid Flow*, Hemisphere Publishing, New York.
- Price, A.G., and Dunne, T. (1976) Energy balance computations of snowmelt in a subarctic area. *Water Resour. Res.* 12, pp. 686-694.
- Rodi, W. (1984) *Turbulence Models and Their Application in Hydraulics*, International Association for Hydraulic Research, Delft, The Netherlands.
- Satterlund, D.R. (1979) An improved equation for estimating long-wave radiation from the atmosphere. *Water Resour. Res.* 15, pp. 1649-1650.
- Shukla, J., and Mintz, Y. (1982) The influence of land-surface evapotranspiration on earth's climate. *Science* 215, pp. 1498-1501.
- Sud, Y.C., Sellers, P.J., Mintz, Y., Chow, M.D., Walker, G.K., and Smith, W.E. (1990) Influence of the biosphere on the global circulation and hydrologic cycle - A GCM simulation experiment. *Agric. For. Meteor.* 52, pp. 133-180.
- Wallace, J.M., and Hobbs, P.V. (1977) *Atmospheric science, an introductory survey*. New York, Academic Press.
- Weller, G., and Holmgren, B. (1974) The microclimates of the arctic tundra. *J. Appl. Met.* 13, pp. 854-862.